Thermal remote sensing in the framework of the SEN2FLEX project: field measurements, airborne data and applications

J. A. Sobrino [a]; J. C. Jiménez-Muñoz [a]; G. Sòria [a]; M. Gómez [a]; A. Barella Ortiz [a]; M. Romaguera [a]; M. Zaragoza [a]; Y. Julien [a]; J. Cuenca [a]; M. Atitar [a]; V. Hidalgo [a]; B. Franch [a]; C. Mattar [a]; A. Ruescas [a]; L. Morales [b]; A. Gillespie [c]; L. Balick [d]; Z. Su [e]; F. Nerry [f]; L. Peres [g]; R. Libonati [g]

[a] Global Change Unit, Department of Earth Physics and Thermodynamics, Faculty of Physics, University of Valencia, 46100 Burjassot, Spain [b] Departamento de Ciencias Ambientales y Recursos Naturales, Facultad de Ciencias Agronomicas, Universidad de Chile, Santiago de Chile, Chile [c] W. M. Keck Remote Sensing Laboratory, Department of Earth and Space Sciences, University of Washington, Seattle, Washington 98195-1310, USA [d] Space and Remote Sensing Sciences Group, Los Alamos National Laboratory, Los Alamos, NM 87545, USA [e] International Institute for Geoinformation Science and Herat Observation (ITC), Enschede, the Netherlands [f] LSIIT/TRIO, Louis Pasteur University, Parc d'innovation, Boulevard Sébastien Brant, BP 10413, F-67412, Illkirch cedex, France [g] Centro de Geofisica da Universidade de Lisboa (CGUL), Campo Grande, 1749-016 Lisbon, Portugal

PLEASE SCROLL DOWN FOR ARTICLE

Thermal remote sensing in the framework of the SEN2FLEX project: field measurements, airborne data and applications

J. A. SOBRINO*†, J. C. JIMÉNEZ-MUÑOZ†, G. SÒRIA†, M. GÓMEZ†,
A. BARELLA ORTIZ†, M. ROMAGUERA†, M. ZARAGOZA†, Y. JULIEN†,
J. CUENCA†, M. ATITAR†, V. HIDALGO†, B. FRANCH†, C. MATTAR†,
A. RUESCAS†, L. MORALES‡, A. GILLESPIE§, L. BALICK¶, Z. SU††,
F. NERRY‡‡, L. PERES§§ and R. LIBONATI§§

†Global Change Unit, Department of Earth Physics and Thermodynamics, Faculty of
Physics, University of Valencia, Dr Moliner 50, 46100 Burjassot, Spain
‡Departamento de Ciencias Ambientales y Recursos Naturales, Facultad de Ciencias
Agronomicas, Universidad de Chile, casilla 1004, Santiago de Chile, Chile
§W. M. Keck Remote Sensing Laboratory, Department of Earth and Space Sciences,
University of Washington, Seattle, Washington 98195-1310, USA
¶Space and Remote Sensing Sciences Group, Los Alamos National Laboratory, Los
Alamos, NM 87545, USA
††International Institute for Geoinformation Science and Herat Observation (ITC),
Enschede, the Netherlands
‡‡LSIIT/TRIO, Louis Pasteur University, Parc d'innovation, Boulevard Sébastien
Brant, BP 10413, F-67412, Illkirch cedex, France
§§Centro de Geofisica da Universidade de Lisboa (CGUL), Campo Grande, 1749-016
Lisbon, Portugal

A description of thermal radiometric field measurements carried out in the
framework of the European project SENtinel-2 and Fluorescence Experiment
(SEN2FLEX) is presented. The field campaign was developed in the region of
Barrax (Spain) during June and July 2005. The purpose of the thermal
measurements was to retrieve biogeophysical parameters such as land surface
emissivity (LSE) and temperature (LST) to validate airborne-based methodol-
ogies and to characterize different surfaces. Thermal measurements were carried
out using two multiband field radiometers and several broadband field
radiometers, pointing at different targets. High-resolution images acquired with
the Airborne Hyperspectral Scanner (AHS) sensor were used to retrieve LST and
LSE, applying the Temperature and Emissivity Separation (TES) algorithm as
well as single-channel (SC) and two-channel (TC) methods. To this purpose, 10
AHS thermal infrared (TIR) bands (8–13 µm) were considered. LST and LSE
estimations derived from AHS data were used to obtain heat fluxes and
evapotranspiration (ET) as an application of thermal remote sensing in the
context of agriculture and water management. To this end, an energy balance
equation was solved using the evaporative fraction concept involved in the
Simplified Surface Energy Balance Index (S-SEBI) model. The test of the
different algorithms and methods against ground-based measurements showed

---

*Corresponding author. Email: sobrino@uv.es

root mean square errors (RMSE) lower than 1.8 K for temperature and lower than 1.1 mm/day for daily ET.

1. Introduction

In the framework of its Earth Observation Envelope Programme, the European Space Agency (ESA) carries out a number of ground-based and airborne campaigns to support geophysical algorithm development, calibration/validation and the simulation of future spaceborne Earth observation (EO) missions.

The SENtinel-2 and FLuorescence EXperiment (SEN2FLEX) is a campaign that combines different activities in support of initiatives related both to fluorescence experiments (AIRFLEX) for observation of solar-induced fluorescence signals over multiple surface targets and to the GMES Sentinel-2 initiative for prototyping spectral bands, spectral widths and spatial/temporal resolutions to meet mission requirements (www.uv.es/~leo/sen2flex/). Both initiatives require simultaneous airborne hyperspectral and ground measurements for interpretation of fluorescence signal levels (AIRFLEX), and simulation of an optical observing system capable of assessing geo- and biophysical variables and classifying target surfaces by spectral, spatial and temporal distinction (Sentinel-2).

Furthermore, the SEN2FLEX campaign includes activities in support of the European Community Water Framework Directive (WFD) EO projects to improve Europe's water resources protection and management.

The main objectives of the SEN2FLEX campaign are: (i) to observe solar-induced fluorescence signals over multiple agricultural and forest targets to verify signal suitability for observations from space as proposed in the FLEX EO mission, (ii) to provide feedback to the ESA on key issues related to ESA's definition of Sentinel-2's multispectral mission requirements, (iii) to validate retrieval algorithms based on hyperspectral and fluorescence signals, and (iv) to provide feedback to the ESA on EO data requirements necessary to fulfil the European Union Water Policy directive. These objectives require the coordinated collection of satellite, airborne hyperspectral and coincident *in situ* data together with analysis of the joint dataset. Two campaigns at different time periods during the year 2005 were carried out to ensure different crop growth stages and conditions: the first on 1, 2 and 3 June 2005 and the second on 12, 13 and 14 July 2005.

Our interest was focused on thermal measurements and Airborne Hyperspectral Scanner (AHS) data analysis to demonstrate the use of thermal infrared (TIR) remote sensing for different environmental applications. In particular, in this paper we present the results obtained in Land Surface Temperature (LST) and Land Surface Emissivity (LSE) retrieval from AHS data. These products (LST and LSE) have been used to estimate the daily evapotranspiration (ET), which provides useful information for water irrigation management. A previous study of LST retrieval from AHS data acquired in 2004 was presented in Sobrino *et al.* (2006). However, in that paper problems with some AHS TIR bands were found, so the analysis was limited to the use of bands 75 to 79 (for technical details of the AHS instrument see section 3.1). As described in section 5, calibration problems were not found in 2005 so we were able to use 10 AHS thermal bands instead of the five bands used in 2004. In addition, some comments and results related to LSE and ET retrieval that were not treated in Sobrino *et al.* (2006) have been included in this paper.

2.   Field measurements

2.1   *Study area*

Field measurements and airborne imagery were collected in the agricultural area of Barrax (39°3′ N, 2°6′ W, 700 m), which is located in Albacete, Spain. The area has been selected in many other experiments because of its flat terrain, minimizing the complications introduced by variable lighting geometry, and the presence of large, uniform land-use units, suitable for validating moderate-resolution satellite image products.

   Barrax has a Mediterranean-type climate, with heavy rainfall in spring and autumn and lighter rainfall in summer; it presents a high level of continentality, with sudden changes from cold months to warm months and high thermal oscillations in all seasons between the maximum and minimum daily temperatures.

   The soils of the area are Inceptisols in terms of soil taxonomy. About 65% of cultivated lands at Barrax are dryland (67% winter cereals, 33% fallow) and 35% irrigated land (75% corn, 15% barley/sunflower, 5% alfalfa, 5% onions and vegetables). The University of Castilla-La Mancha, through the 'Escuela Técnica Superior de Ingenieros Agrónomos', operates three agro-meteorological stations in the study area. More details about the test site are presented in Moreno *et al.* (2001). Figure 1 shows an index map of the study area and the plots where measurements were made.

2.2   *Instrumentation*

Various instruments were used to measure in the TIR domain, including multiband and single-band radiometers with a fixed field-of-view (FOV). Calibration processes
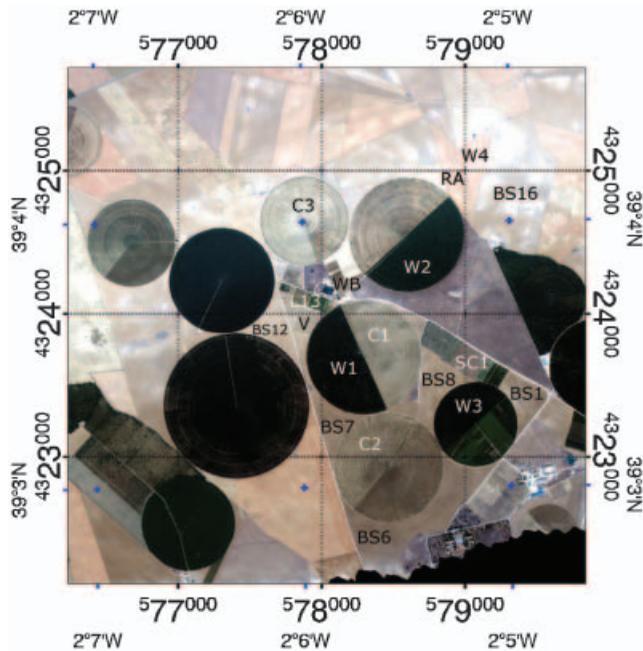

Figure 1.   Barrax study area and location of parcels where thermal infrared measurements were performed. Crops are distributed in circles for irrigation purposes.

were carried out with the use of calibration sources (black bodies). The instruments used are summarized in table 1.

The CIMEL detectors CE-312-1 and CE312-2 are two radiance-based TIR radiometers comprising an optical head and a data storage unit. CE312-1 includes one broadband filter (8–13 µm) and three narrower filters (8.2–9.2, 10.5–11.5 and 11.5–12.5 µm). CE312-2 includes six bands, a wide one (8–13 µm) and five narrower filters (8.1–8.5, 8.5–8.9, 8.9–9.3, 10.3–11 and 11–11.7 µm). The temperature of an external black body can be measured with a temperature probe. One CIMEL CE312-1 and two CIMEL CE312-2 detectors were used during the field campaign. The two portable RAYTEK ST6 radiometers, a standard model and a ProPlus model, were also used. They have a single band at 8–14 µm, and a FOV of 7° and 2°, respectively. They cover a temperature range from −32°C to 400°C with a sensitivity of 0.1 K and an accuracy of 1 K. A built-in laser beam helps users to aim at the target. Three Raytek Thermalert MID radiometers with different FOVs (6° and 30°) were used. They have an IR sensor with a single band at 8–14 µm, a temperature range from −40°C to 600°C, and a sensitivity of 0.5 K and an accuracy of 1 K. Four different Licor LI-1000 dataloggers were used to store data from the radiometers set up on masts.

Additional IR radiometers were also used in the field campaign: five portable OPTRIS MiniSight Plus (with laser beam) IR radiometers, with a single band at 8–14 µm, a FOV of 3°, a temperature range from −32°C to 530°C and with a sensitivity of 0.7 K and an accuracy of 1 K; an Oakton Temp Testr I portable radiometer, with a single band at 8–14 µm, a sensitivity of 0.5 K and an accuracy of 2 K, with fixed emissivity value set to 1; and two Everest radiometers model 4000, with a FOV of 15°.

Two thermal cameras were used during the field campaign. The Irisys-Iri1011 TIR camera has a single band at 8–14 µm, with an instantaneous FOV (IFOV) of

Table 1. Technical specifications for the instruments.

Instrument	Spectral range (µm)	Temperature range (K)	Accuracy (K)	Resolution	FOV
Cimel CE312-1	8–13	193–323	0.1	8 mK	10°
	11.5–12.5			50 mK	
	10.5–11.5			50 mK	
	8.2–9.2			50 mK	
Cimel CE312-2	8–13	193–333	0.1	8 mK	10°
	11–11.7			50 mK	
	10.3–11			50 mK	
	8.9–9.3			50 mK	
	8.5–8.9			50 mK	
	8.1–8.5			50 mK	
Raytek MID	8–14	233–873	1	0.5 K	30° (6°)
Raytek ST	8–14	241–673	1	0.1 K	7–2°
Everest 3000.4	8–14	243–373	0.5	0.1 K	4°
Optris minisight	8–14	241–803	1	0.7 K	3°
NEC TH9100	8–14	313–393	2	0.1 K	22° × 16°
Irisys Iri-1011	8–14	263–573	2	0.5 K	20° × 20°
Calibration sources					
EVEREST 1000		Fixed to ambient	0.3	0.1 K	
GALAI 204-P		Variable (273–373)	0.2	0.1 K	

20° and adjustable emissivity operation mode. It covers a temperature range from −10°C to 300°C with a sensitivity of 0.5 K. The NEC Thermo Tracer TH9100 Pro thermal camera has a single band at 8–14 μm, with an IFOV of $22° \times 16°$ and adjustable emissivity operation mode. It ranges from −40°C up to 120°C with a sensitivity of 0.1 K. A visible image can also be acquired simultaneously to the thermal image.

Two calibration sources were used to calibrate the radiometers: a calibration source EVEREST model 1000 with operating range 0–60°C, a sensitivity of 0.1 K and an absolute accuracy of 0.3 K over the entire range; and the calibration source GALAI model 204-P with operating range 0–100°C, a sensitivity of 0.1 K and an absolute accuracy of 0.2 K over the entire range.

A diffuse reflectance standard plate, model Labsphere Infragold, was used to estimate the sky irradiance.

2.3 *Radiometric temperatures*

A set of thermal radiometric measurements was carried out over different plots. Figure 1 shows the parcels where different measurements where carried out, where BS is bare soil, W is wheat, L is the lysimeter field (green grass), WB is water body, C is corn, RA is reforestation area (senescent vegetation), SC is small corn and V is vineyard.

Prior to the radiometric measurements, a calibration was carried out to compare each instrument with the reference black body sources. Raytek MID and EVEREST radiometers were used for continuous recording of surface brightness temperature as a function of time in different locations. CIMEL radiometers, Raytek ST and OPTRIS portable radiometers were used mainly for transects over different samples.

Transects were carried out over selected surfaces, concurrently to the plane overpass, starting half an hour before and ending half an hour after. Brightness temperatures were measured with field radiometers, at regular steps (∼3 m) along a walk performed within a well-defined area. Measurements of sky downwelling radiance were also performed.

Radiometric temperatures were recorded continuously with radiometers located on fixed masts over determined areas and periods of time. Figure 2 shows the temporal evolution of radiometric temperature of different samples (bare soil, wheat, green grass) in the course of the first SEN2FLEX campaign (June). Air temperature measured with a thermocouple is also represented.

2.4 *Thermal pictures*

The TH9100 thermal camera was used to characterize different crops in the region of study (figure 3). Temporal series were acquired over selected samples and thermal imaging of parcels was carried out during plane overpasses. Thermal imagery was also taken with the Irisys thermal camera to study spatial variation of radiometric temperature for different samples (figure 4).

2.5 *Emissivity spectra*

Surface emissivities were obtained from ground-based measurements applying the Temperature and Emissivity Separation (TES) algorithm (Gillespie *et al.* 1998) to data measured with the CIMEL CE312-2 instrument (Jiménez-Muñoz and Sobrino 2006). Different emissivity spectra included in the Advanced Spaceborne Thermal
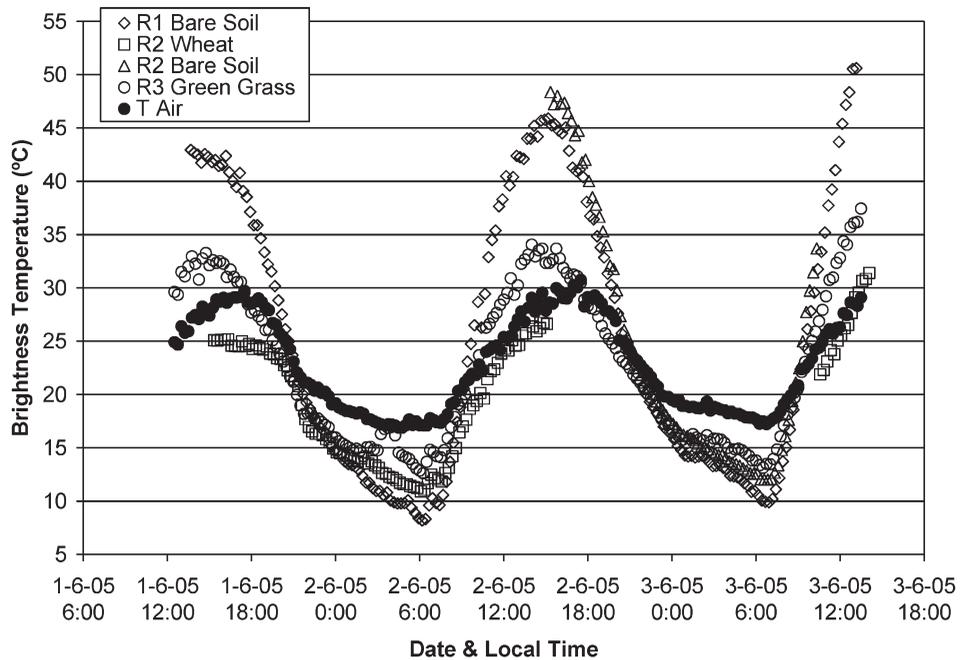
Figure 2. Continuous measurements of brightness temperature with Raytek Thermalert MID (R) radiometers on masts. Air temperature (T Air) measured with a thermocouple is also represented.

Emission and Reflection Radiometer (ASTER) spectral library (http://speclib.jpl. nasa.gov/) were also used to retrieve band emissivities for the AHS thermal bands. The emissivity spectrum for a sample of soil was also measured in the Jet Propulsion Laboratory. Some results are presented in section 4.

3.   The Airborne Hyperspectral Scanner (AHS)

3.1   *Technical characteristics*

The AHS (developed by SensyTech Inc., currently ArgonST, USA) is operated by the Spanish Institute of Aeronautics (INTA), onboard its aircraft CASA 212-200 Paternina. The AHS incorporates advanced components to ensure high performance while maintaining the ruggedness to provide operational reliability in a survey aircraft. The main AHS technical specifications are:

- Optical design: scan mirror plus Cassegrain-type afocal telescope with a single IFOV determining field stop (Pfund assembly)
- FOV/IFOV: 90°/2.5 mrad
- Ground sampling distance (GSD): 2.1 mrad (0.12°)
- Scan rates: 12.5, 18.75, 25 and 35 Hz, with corresponding ground sampling distances from 7 to 2 m
- Digitization precision: 12 bits to sample the analogue signal, with gain level from ×0.25 to ×10
- Samples per scan line: 750 pixels/line
- Reference sources: two controllable thermal black bodies ('cold' and 'hot') placed at the edges of the FOV acquired for each scanline

L13 (Grass) VISIBLE

W1 (Wheat) VISIBLE

L13 (Grass) THERMAL (daytime)

W1 (Wheat) THERMAL (daytime)

L13 (Grass) THERMAL (night-time)

W1 (Wheat) THERMAL (night-time)

Figure 3. Visible and thermal imagery obtained with the NEC camera over parcels L13 (green grass) and W1 (wheat) during the day and night-time.

- Spectrometer: four dichroic filters to split radiation in four optical ports [visible/near-IR (VIS/NIR), shortwave IR (SWIR), mid-IR (MIR) and TIR], and diffraction gratings within each port, plus lens assemblies for refocusing light onto the detectors
- Detectors: Si array for VIS/NIR port; InSb and MCT arrays, cooled in N_2 dewars, for SWIR, MIR and TIR ports

J. A. Sobrino et al.

Figure 4.   Thermal imaging with the Irisys camera over (*a*) bare soil, which shows a thermal amplitude of 12 K and a standard deviation of 2.4 K, and (*b*) grass, with a thermal amplitude of 8 K and a standard deviation of 1.3 K.

- Spectral bands: continuous coverage in four spectral regions + single band at 1.5 μm, as shown in table 2
- Noise Equivalent Delta-Temperature (NEΔT) for TIR bands ~0.25°C (depends on the band considered)

Table 2. AHS spectral configuration.

	PORT 1	PORT 2A	PORT 2	PORT 3	PORT 4
Coverage (µm)	0.43–1.03	1.55–1.75	2.0–2.54	3.3–5.4	8.2–12.7
FWHM (µm)	28	200	13	30	400–500
$\lambda/\Delta\lambda$ (minimum)	16	8	150	110	160
Number of bands	20	1	42	7	10

Effective wavelengths for the AHS thermal bands from 71 to 80 (which are the main bands used in this paper) are 8.18, 8.66, 9.15, 9.60, 10.07, 10.59, 11.18, 11.78, 12.35 and 12.93 µm.

3.2 *Imagery dataset*

During the SEN2FLEX campaign the AHS flights took place on 1, 2 and 3 June 2005 and 12, 13 and 14 July 2005, with a total of 24 AHS images (four flights each day). Flights were made at three different altitudes (975, 2070 and 2760 m above sea level) and at different times (ranging from 0800 to 1230 UTM, including two night-time acquisitions at 2200 and 2230 UTM on 12 July 2005). The description of the different flights is given in table 3.

Table 3. Description of the AHS flights carried out in the SEN2FLEX campaign. Altitude refers to the height of the flights above sea level.

Date (yymmdd)	Time (UTM)	Flight ID	Altitude (m)	w (g cm^{-2})	Pixel size (m)
050601	11:23	BDS	1675 (975)	0.37	2
050601	11:48	MDS	2070 (1370)	0.51	3
050601	12:11	I1	2760 (2060)	0.74	4
050601	12:33	I2	2760 (2060)	0.74	4
050602	11:19	BDS	1675 (975)	0.41	2
050602	11:41	MDS	2070 (1370)	0.57	3
050602	12:03	I1	2760 (2060)	0.83	4
050602	12:25	I2	2760 (2060)	0.83	4
050603	11:11	BDS	1675 (975)	0.61	2
050603	11:34	MDS	2070 (1370)	0.79	3
050603	11:57	I1	2760 (2060)	1.10	4
050603	12:19	I2	2760 (2060)	1.10	4
050712	11:56	BDS	1675 (975)	0.80	2
050712	12:21	MDS	2070 (1370)	0.99	3
050712	22:07	BNS	1675 (975)	0.48	2
050712	22:32	MNS	2070 (1370)	0.63	3
050713	7:52	B1S	1675 (975)	0.61	2
050713	8:15	M1S	2070 (1370)	0.84	3
050713	11:46	B2S	1675 (975)	0.58	2
050713	12:01	M2S	2070 (1370)	0.74	3
050714	8:03	B1S	1675 (975)	0.58	2
050714	8:23	M1S	2070 (1370)	0.74	3
050714	12:06	B2S	1675 (975)	0.48	2
050714	12:25	M2S	2070 (1370)	0.63	3

Altitude above ground level is given in parentheses.
w, atmospheric water vapour content calculated from atmospheric soundings launched near the AHS overpass and for the flight altitudes.

3.3 *Processing and atmospheric correction*

The INTA team provided the AHS imagery processed to at-sensor radiances, and also the Image Geometry Model (IGM) files needed to perform the geometric correction.

The atmospheric correction of the AHS visible and near-infrared (VNIR) data (bands from 1 to 20) was performed by an automatic method developed at the University of Valencia (Guanter *et al.* 2005), from which the at-sensor radiance is transformed to at-surface reflectivities. It is based on the retrieval of atmospheric constituents (aerosol and water vapour content) from the data themselves. All atmospheric calculations are based on MODTRAN4 (Berk *et al.* 1999) calculations carried out during each image processing. The dependence of the atmospheric optical parameters on the scan angle is accounted for by a polynomial fitting technique that performs a quadratic interpolation between a set of tabulated breakpoints giving the atmospheric parameters as a function of the scan angle.

Atmospheric correction of the AHS TIR bands (71 to 80) was performed considering the radiative transfer equation:

$$L_i(T_i) = L_i^{\mathrm{LLR}}\tau_i + L_i^{\uparrow} \tag{1}$$

where $L_i(T_i)$ is the radiance measured by the sensor (T_i is the at-sensor brightness temperature), τ_i the atmospheric transmissivity and $L_i^{\uparrow}$ the upwelling path radiance. The term L^{LLR} is the land-leaving radiance (LLR) or radiance measured at ground level, which is given by:

$$L_i^{\mathrm{LLR}} = \varepsilon_i B_i(T_s) + (1-\varepsilon_i)\frac{F_i^{\downarrow}}{\pi} \tag{2}$$

where ε_i is the surface emissivity, $B_i(T_s)$ is the Planck radiance at surface temperature T_s, and $F_i^{\downarrow}$ is the downwelling sky irradiance. In equation (2) the assumption of lambertian behaviour for the surface has been considered in order to express the reflection term as $(1-\varepsilon)\pi^{-1}F^{\downarrow}$. The magnitudes involved in equations (1) and (2) are band-averaged values using the spectral response functions, and also depend on the observation angle. Then, the atmospheric correction in the TIR region is reduced to:

$$L_i^{\mathrm{LLR}} = \frac{L_i(T_i) - L_i^{\uparrow}}{\tau_i} \tag{3}$$

The atmospheric parameters τ_i, $F_i^{\downarrow}$ and $L_i^{\uparrow}$ involved in the above equations were estimated using the MODTRAN-4 radiative transfer code and *in situ* radio-soundings launched almost simultaneously with the AHS overpass. Band values were finally obtained using AHS TIR band filter functions. These filter functions as well as a comparison with atmospheric transmissivity are presented in Sobrino *et al.* (2006). That work showed that AHS bands 71 and 80, located around 8 and 13 μm, respectively, present the highest atmospheric absorption, whereas band 74 is located in the region of ozone absorption (even though at the altitude of the AHS flights this absorption is not observed). Therefore, the *a priori* optimal bands for TIR remote sensing are 72, 73, 75, 76, 77, 78 and 79.

4. Vicarious calibration of the AHS thermal bands

Before the application of the different algorithms, it is convenient to compare data provided by the sensor with data acquired *in situ*. In this way, technical or

calibration problems of the AHS sensor can be detected. According to Toonoka *et al.* (2005), the conditions required for calibration sites are: (i) targets should be homogeneous in both surface temperature and emissivity, and (ii) atmospheric conditions should be stable and cloud-free, with a small total amount of water vapour. In this study, and to show the problems related to the heterogeneity of the surface, we have also included heterogeneous targets. From all the measurements collected in the field and presented in section 2, a total amount of 97 test points were considered in the vicarious calibration and also in the algorithms testing (as shown in section 5). These measurements were collected over water body (WB), corn (C1 and C2), green grass (L13), bare soil (BS1, BS6, BS7, BS8, BS12 and BS16) and vineyard (V) (see figure 1).

At-sensor radiances for each AHS TIR band have been reproduced from ground-based measurements using equations (1) and (2). Surface temperatures (T_s in equation (2)) were obtained from measurements carried out with broadband radiometers after broadband emissivity correction (assumed to be 0.97 for bare soil and 0.99 for water and green vegetation) and downwelling atmospheric radiance (measured with the diffuse reflectance standard plate). As explained in section 3.3, atmospheric parameters were obtained with MODTRAN-4 and atmospheric soundings. Emissivity spectra for water and green grass were extracted from the ASTER spectral library (http://speclib.jpl.nasa.gov), and the bare soil emissivity spectrum was measured in the Jet Propulsion Laboratory (www.jpl.nasa.gov) from a sample collected in the field (the measurement procedure is described at http://speclib.jpl.nasa.gov/documents/jpl_desc.htm). A constant value of 0.99 was assumed for the corn plot, unlike the vineyard case, where an average value between bare soil and 0.99 was considered. Figure 5 shows the AHS band emissivities for different plots.
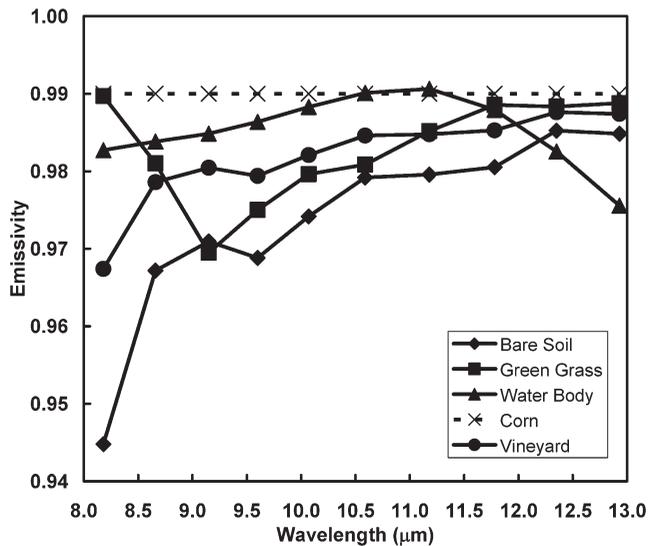

Figure 5. Emissivity values for the 10 AHS TIR bands (from 71 to 80) used in the vicarious calibration. They were obtained from emissivity spectra included in the ASTER spectral library (water body and green grass) or measured in the laboratory (bare soil, measured at the Jet Propulsion Laboratory). A constant value of 0.99 was assumed for the corn plot (fully covered) and average values of bare soil and vegetation (0.99) were considered for the vineyard.

A comparison between at-sensor values measured with the AHS and those reproduced from ground-based measurements was made for the 97 test points. Figures 6–10 show some illustrative examples of the results obtained over water body, corn, green grass, bare soil and vineyard plots, respectively. The comparison is presented in terms of at-sensor brightness temperatures. Some basic statistics such as bias, standard deviation and root mean square errors (RMSE) are given. These statistics refer to differences between AHS and measured (*in situ*) values for the 10 AHS TIR bands. In general, the shape of the spectra obtained from ground-based measurements agrees with those extracted from the AHS images, which *a priori* indicates that the AHS TIR bands do not have technical problems, as was found in the SPARC 2004 campaign (Sobrino *et al.* 2006). As expected, the best results are obtained for the water body (figure 6), with RMSE values below 1 K, as this plot is the most homogeneous (in terms of temperature and emissivity). Despite the corn plot being fully covered (figure 7), which could also be considered as homogeneous, some heterogeneities were found, as shown by the high error bars of *in situ* values (>3 K). This is probably due to soil influence in the field radiometers' FOV, which is minimized at sensor level. Some significant discrepancies were also found for the green grass plot (figure 8). Despite this plot being labelled as 'green', some areas of
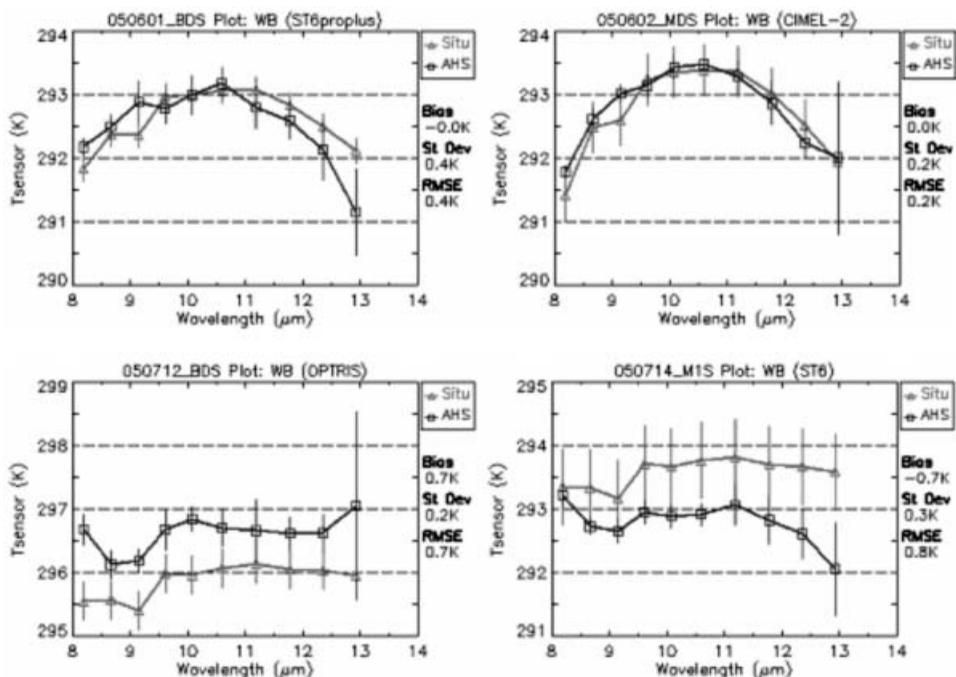

Figure 6. Comparison between the at-sensor brightness temperatures measured with the 10 AHS TIR bands (from 71 to 80) and the temperatures reproduced from ground-based measurements (Situ) for water body. Error bars for 'Situ' values refer to the standard deviation of the different field measurements collected near the AHS overpass, and error bars for 'AHS' values refer to the standard deviation of sampled 3 × 3 pixels. The top of the graphs show date, flight ID (see table 2), plot and name of the field radiometer used to measure surface temperature (in parentheses). On the right of each graph, values of bias (mean value for the difference between AHS values and the values measured *in situ*, for the 10 AHS TIR bands), standard deviation (St Dev) and root mean square errors (RMSE) are given.
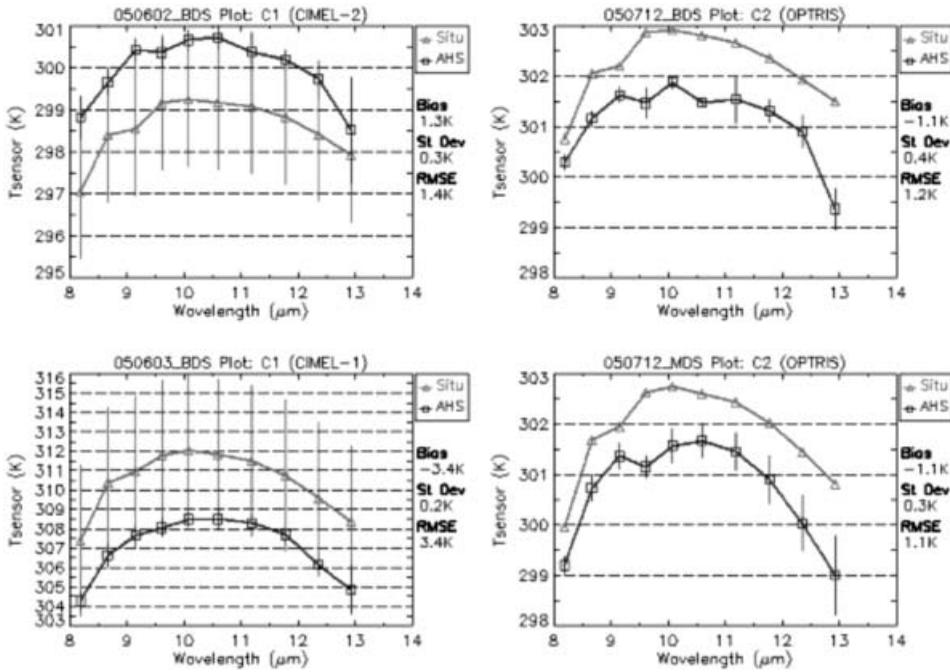
Figure 7. Comparison between the at-sensor brightness temperatures measured with the 10 AHS TIR bands (from 71 to 80) and the temperatures reproduced from ground-based measurements (Situ) for the corn (fully-covered) plot. See figure 6 for further details.
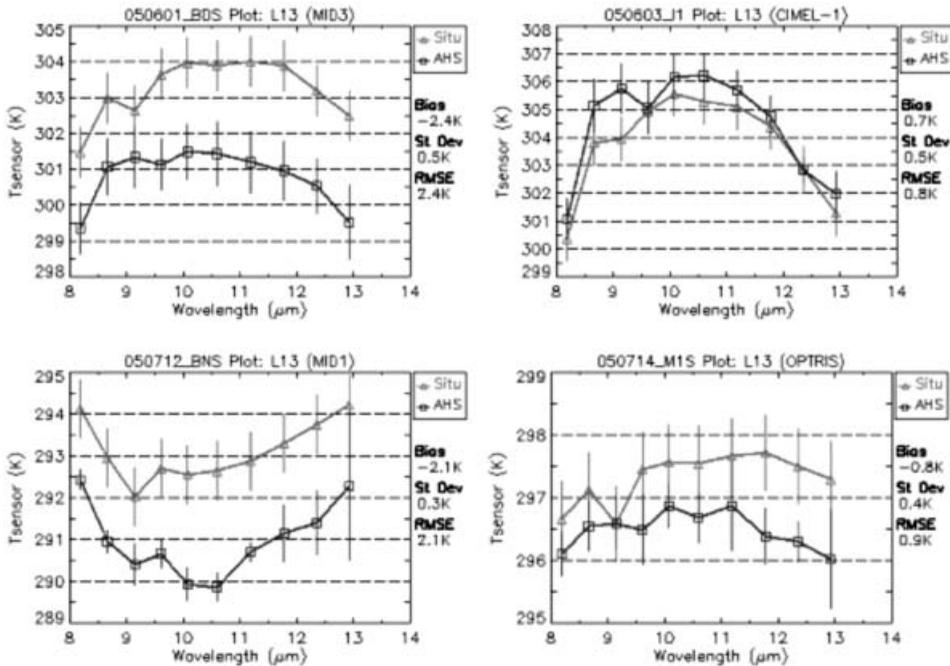

Figure 8. Comparison between the at-sensor brightness temperatures measured with the 10 AHS TIR bands (from 71 to 80) and the temperatures reproduced from ground-based measurements (Situ) for the green grass (L13) plot. See figure 6 for further details.

dry grass are also visible. The results obtained over the bare soil plot (figure 9) are typically good (RMSE≈1 K). However, significant differences (>2 K) were obtained in some cases. Following Balick *et al.* (2003), these differences could be attributed to turbulence-induced temperature changes at the surface (also presented over the canopy, although to a lesser degree). The worst results were obtained for the vineyard (figure 10), which is expected because of the high degree of heterogeneity of this plot (composed of soil, trunks and leaves, differences between sunlit and shadowed leaves, etc.). The results were good (RMSE=0.7 K) for the night-time flight (050712_MNS), probably because of the thermal homogeneity achieved during this time, with similar temperatures for soil and vegetation and without shadows.

To assess the overall accuracy in the comparison between AHS and *in situ* data, figure 11 shows the results obtained for all of the test points measured in each plot, including values for the 10 AHS TIR bands. One of the graphs in figure 11 shows all the test points, without distinction between plots. The RMSE values for water body, corn, green grass, bare soil and vineyard plots are below 0.9, 1.8, 1.9, 1.9 and 2.2 K, respectively. An overall RMSE<1.5 K has been finally obtained for the 97 test points and for the 10 AHS TIR bands.

5. Applications

Land surface processes may be loosely defined as those attributes, exchanges and relationships that contribute to the overall functioning of the concomitant physical, biophysical and hydrological interactions that come together to form the landscape.

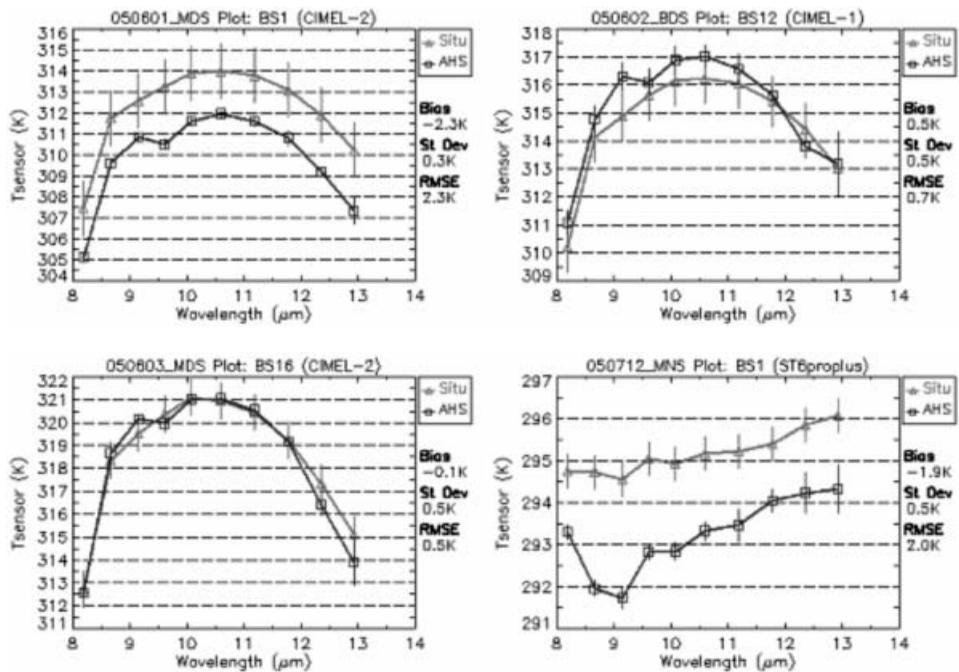

Figure 9. Comparison between the at-sensor brightness temperatures measured with the 10 AHS TIR bands (from 71 to 80) and the temperatures reproduced from ground-based measurements (Situ) for the bare soil plot. See figure 6 for further details.
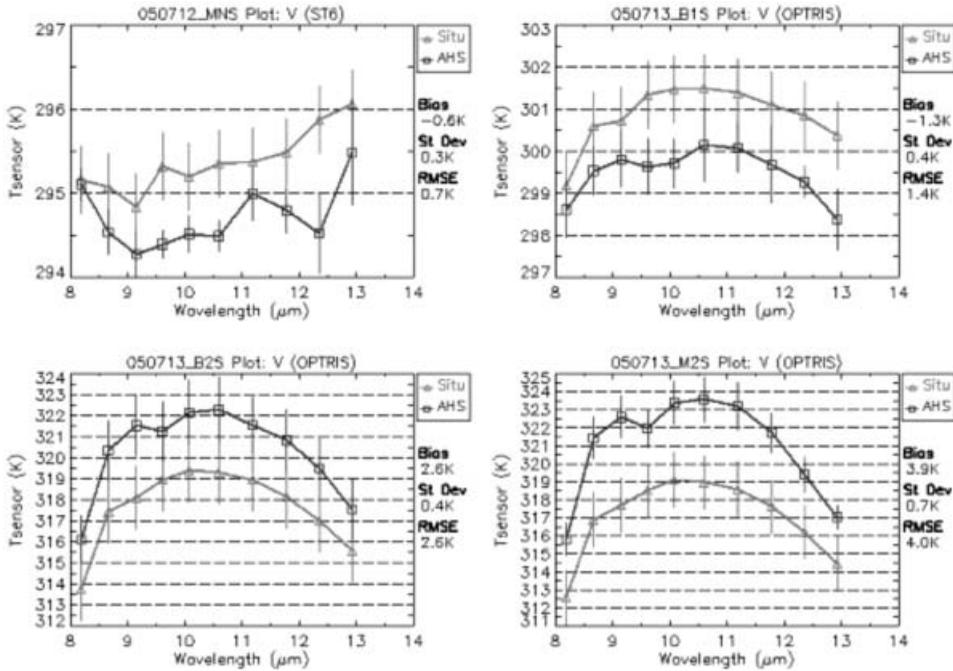
Figure 10. Comparison between the at-sensor brightness temperatures measured with the 10 AHS TIR bands (from 71 to 80) and the temperatures reproduced from ground-based measurements (Situ) for the vineyard plot. See figure 6 for further details.

These include the processes that occur across the land surface as well as between the land surface and the atmosphere. Using this definition as a foundation or a baseline, there are two fundamental reasons why TIR data contribute to an improved understanding of land surface processes: (i) through measurement of surface temperatures as related to specific landscape and biophysical components and (ii) through relating surface temperatures to energy fluxes for specific landscape phenomena or processes (Quattrochi and Luvall 1999). These statements highlight the importance of TIR remote sensing for different environmental studies. In particular, this section presents different algorithms for LST and LSE retrieval, and also a simple methodology to estimate ET, which is an important parameter for water irrigation management. It should be noted that although the algorithms mainly use AHS TIR bands, the AHS VNIR bands is also used for retrieval of complementary parameters. This also highlights the importance of the synergistic use of optical and thermal remote sensing.

5.1 *LST and emissivity retrieval*

LST retrieval algorithms are based on the radiative transfer equation given by equations (1) and (2), which can be combined to give:

$$L_i(T_i) = \left[\varepsilon_i B_i(T_s) + (1 - \varepsilon_i) L_i^{\downarrow} \right] \tau_i + L_i^{\uparrow} \tag{4}$$

where $L^{\downarrow}$ refers to the downwelling sky irradiance divided by π. As can be observed in equation (4), there is a coupling between emissivity and temperature, so that knowledge of surface emissivities is required to obtain accurate values of the LST.
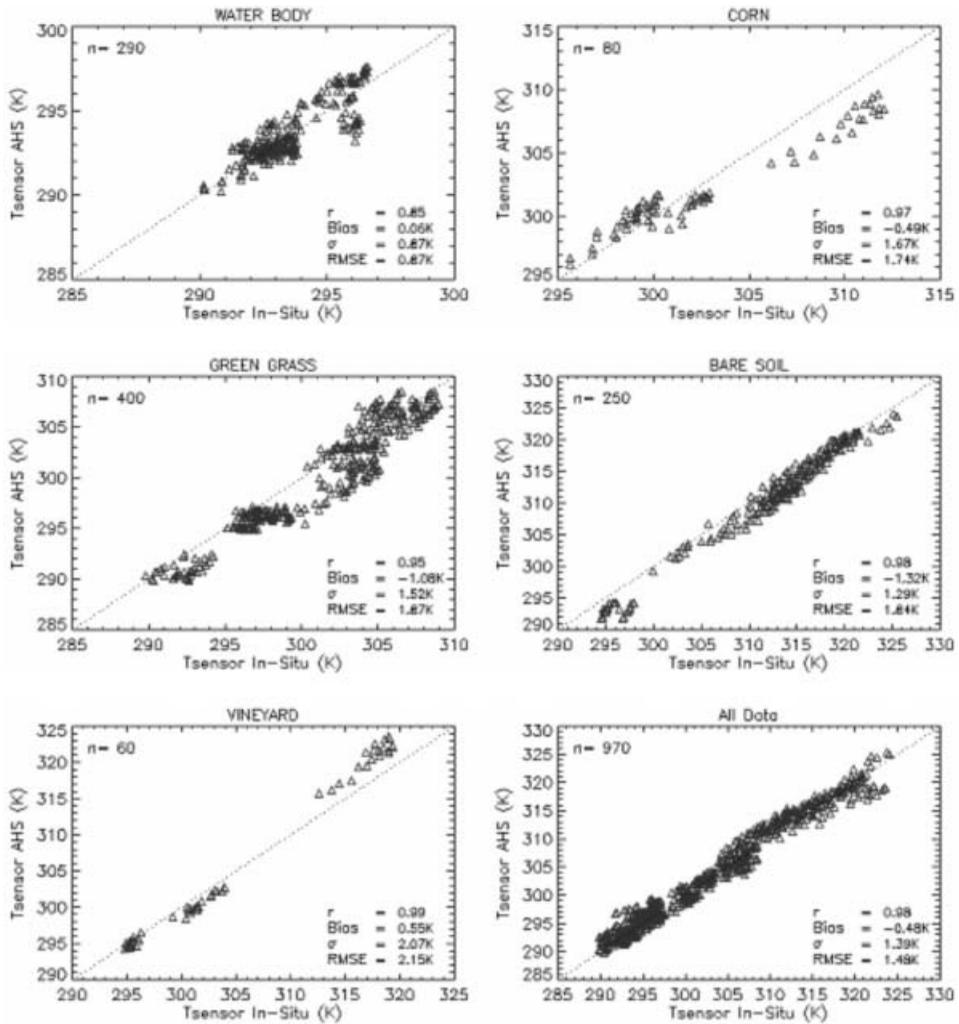
Figure 11. Similar to Figure 6, but in this case all the measurements carried out over each test point and for the 10 AHS TIR bands are put together to show the overall accuracy for each particular plot. The last graph includes all the test points. Values of correlation (r), bias, standard deviation (σ) and root mean square errors (RMSE) are also given. The number of points represented in the graphs (n) refers to the number of test points multiplied by the number of AHS TIR bands (10).

Surface emissivities *per se* are also useful for environmental studies, as for example in mineralogical mapping. In the following subsections we show different operational methods for retrieving both surface temperatures and emissivities.

5.1.1 Single-channel (SC) method assuming a constant value for emissivity. The first method proposed for LST retrieval from AHS data is the SC method, which is based on the inversion of the radiative transfer equation (4):

$$T_s = B^{-1}\left(\frac{L_i(T_i) - L_i^{\uparrow}}{\tau_i \varepsilon_i} - \frac{(1-\varepsilon_i)}{\varepsilon_i} L_i^{\downarrow}\right) \tag{5}$$

This is *a priori* the simplest method as it uses only one TIR band. We have also assumed a constant value for emissivity of 0.98, which further simplifies the application method. The atmospheric parameters in equation (5) were obtained from MODTRAN-4 and atmospheric soundings. The relationships between these parameters and the atmospheric water vapour content (which can be measured or retrieved from remote sensing data) can also be considered, as described in Sobrino *et al.* (2006). The optimal AHS TIR band for application of the SC algorithm was selected according to the highest atmospheric transmissivity value. In all of the atmospheric conditions during the SEN2FLEX campaign, the AHS band 75 (10.07 μm) provided the highest transmissivity, as shown in figure 12, so this band was finally selected. The results obtained were validated against the 97 test points mentioned in section 4 (see figure 13). The values retrieved with the SC method and those measured *in situ* are well correlated ($r=0.98$) and with low bias (-0.4 K, where the negative sign indicates an underestimation of the SC method). The RMSE value is below 1.7 K, which agrees with typical errors in the LST retrieval (e.g. Gillespie *et al.* 1998, Sobrino and Raissouni 2000, Kerr *et al.* 2004, Sobrino and Jiménez-Muñoz 2005, Sobrino *et al.* 2006, 2007).

5.1.2 Two-channel (TC) technique and emissivity retrieval from the Normalized Difference Vegetation Index (NDVI). The second method proposed for LST retrieval is the TC technique, also called Split-Window (SW) when working in 10–12 μm, which has been widely used by the scientific community (e.g. Kerr *et al.* 2004). In this case we have considered the TC algorithm proposed by Sobrino and Raissouni (2000):

$$T_s = T_i + a_1(T_i - T_j) + a_2(T_i - T_j)^2 + a_0 + (a_3 + a_4 w)(1 - \varepsilon) + (a_5 + a_6 w)\Delta\varepsilon \quad (6)$$
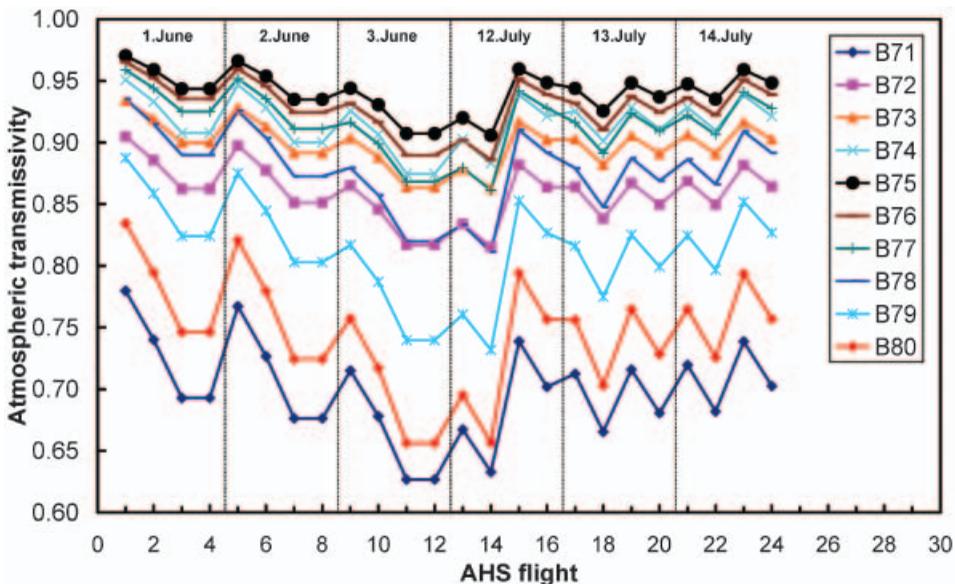

Figure 12. Atmospheric transmissivity values for each AHS thermal band and for flights performed during the SEN2FLEX campaign, obtained with MODTRAN4 and atmospheric soundings.
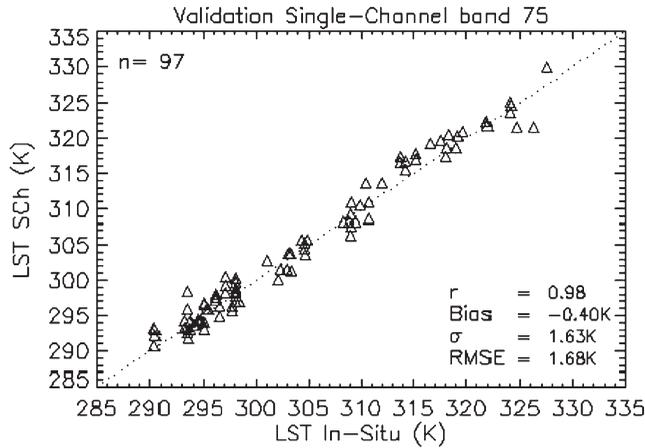
Figure 13. Validation of the Single-Channel method (LST SCh) against 97 *in situ* measurements (LST In-Situ) over different crops and for different dates.

where T_i and T_j are the at-sensor brightness temperatures (in K) for two different AHS TIR bands, w is the atmospheric water vapour content (in g/cm^2) and $\varepsilon = 0.5(\varepsilon_i + \varepsilon_j)$ and $\Delta\varepsilon = (\varepsilon_i - \varepsilon_j)$ are, respectively, the mean emissivity and the emissivity difference for the two AHS bands considered. As can seen, this method requires two TIR bands. The coefficients a_i ($i = 0$–6) are obtained from simulated data (atmospheric soundings, MODTRAN-4 and emissivity spectra), as explained in Sobrino *et al.* (2006). In this case, 61 atmospheric soundings and 108 emissivity spectra extracted from the ASTER spectral library (soils, vegetation, water, ice and whole rock chips) were used. AHS TIR bands 75 (10.07 μm) and 79 (12.35 μm) were selected to apply to equation (6) because, according to the sensitivity analysis presented in Sobrino *et al.* (2006), this combination of bands provides the best results. Table 4 shows the numerical coefficients obtained for the different AHS flight altitudes (see table 3), and table 5 shows the errors expected for the TC algorithm according to the sensitivity analysis.

Taking into account the fact that the atmospheric water vapour (w) can be extracted from atmospheric soundings (see values in table 3) or can be measured *in situ* or obtained from remote sensing data, we need to estimate the land surface emissivity to apply equation (6) in an operational way. In this case we considered the following simplified approach:

$$\varepsilon_i = \varepsilon_{s,i}(1 - \text{FVC}) + \varepsilon_{v,i}\text{FVC} \tag{7}$$

where ε_s is the soil emissivity (obtained from the spectrum measured at the Jet

Table 4. Coefficients for the Two-Channel algorithm given by equation (6) and using AHS bands 75 and 79. The coefficients are given for three different altitudes, according to the AHS flights performed during the SEN2FLEX campaign (see table 2).

Flight	a_0	a_1	a_2	a_3	a_4	a_5	a_6
B	−0.0028	0.59776	0.04231	44.77	−8.41	−54.39	25
M	−0.033	0.68815	0.04266	44.73	−6.2	−59.09	21.45
I	−0.08463	0.723	0.04275	45.49	−5.17	−60.81	16.93

Table 5. Errors obtained in the sensitivity analysis of the Two-Channel algorithm using AHS bands 75 and 79.

Flight	σ (K)	r	e-NEΔT (K)	e-ε (K)	e-W (K)	RMSE (K)
B	0.2	0.98	0.17	0.6	0.4	0.8
M	0.2	0.98	0.19	0.6	0.4	0.8
I	0.2	0.98	0.2	0.6	0.3	0.8

σ, standard error of estimation; r, correlation coefficient; e-NEΔT, error due to Noise Equivalent Delta-Temperature; e-ε, error due to uncertainty in the emissivity; e-W, error due to uncertainty in the atmospheric water vapour; RMSE, root mean square error for the 61×108 cases in which the sensitivity analysis was performed.

Propulsion Laboratory, see figure 5), ε_v is the vegetation emissivity (assumed to be a constant value of 0.99) and FVC is the fractional vegetation cover estimated from the NDVI according to Carlson and Ripley (1997):

$$FVC = \left[\frac{NDVI - NDVI_s}{NDVI_v - NDVI_s} \right]^2 \tag{8}$$

where $NDVI_s$ is the soil NDVI and $NDVI_v$ the vegetation NDVI, estimated from the NDVI histogram. This methodology has proved to be adequate over agricultural areas, as presented, for example, in Jiménez-Muñoz *et al.* (2006).

The TC algorithm (using surface emissivities estimated from the NDVI as input) was also validated against 97 test points, and the results are shown in figure 14. A similar bias to that in the previous case (SC method) was obtained, 0.4 K (in this case with an overestimation of the TC algorithm), with a slightly higher standard deviation, leading to a final RMSE of 1.8 K.

Figures 15 and 16 show, respectively, some illustrative land surface emissivity (AHS band 75) and temperature maps for the four AHS flights made on 1 June 2005 (see table 3 for flights details). Figure 15 shows emissivity values for AHS band 75 ranging from 0.97 (soil) to 0.99 (vegetation), which justifies the selection of a constant value of 0.98 in the SC method presented in section 5.1.1. This figure also
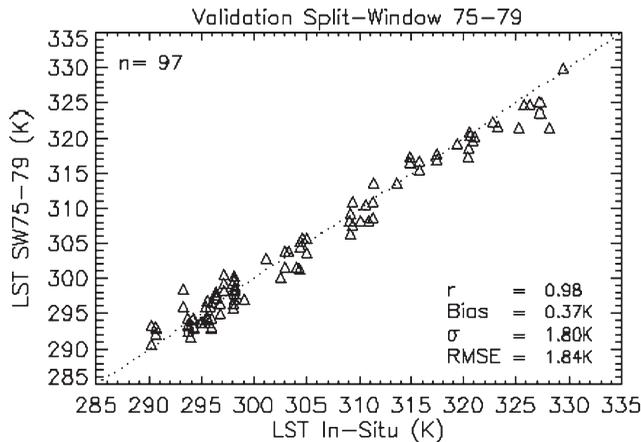

Figure 14. Validation of the Split-Window algorithm using AHS bands 75 and 79 (LST SW75–79) against 97 *in situ* measurements (LST In-Situ) over different crops and for different dates.
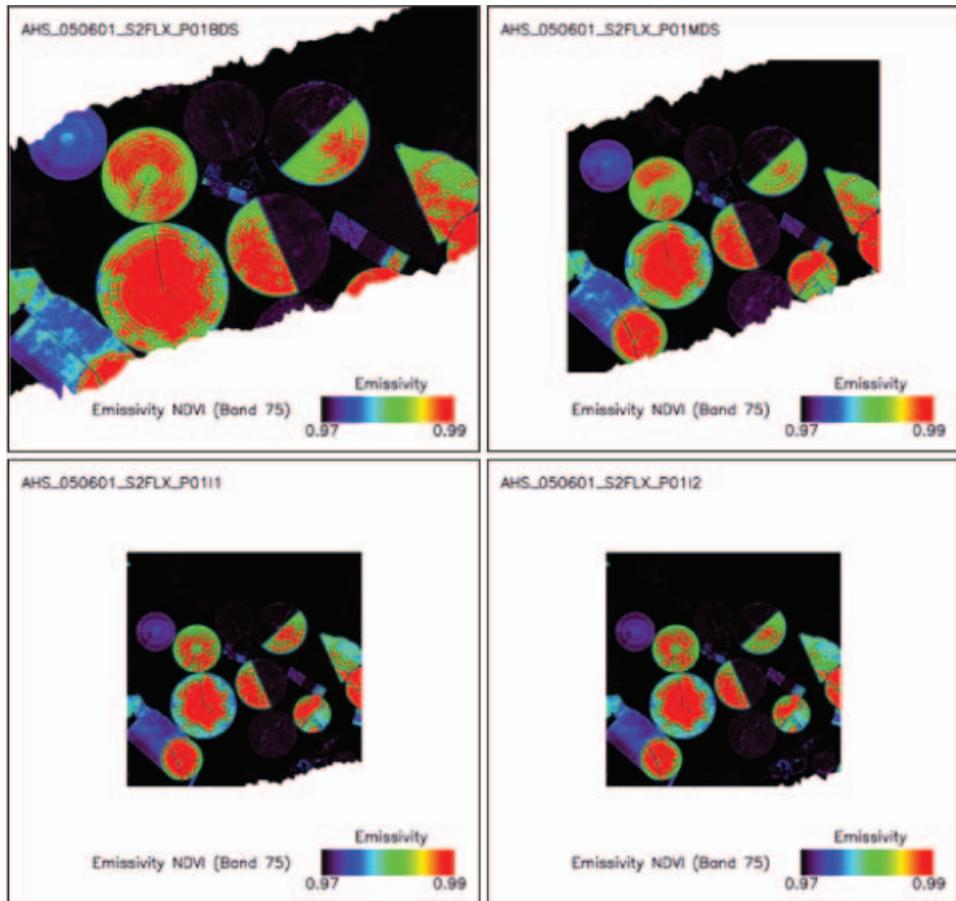
Figure 15.   Land surface emissivity maps for AHS band 75 obtained with the NDVI.

shows some variations in emissivity inside the circular crops, which highlights the presence of some heterogeneities over areas previously considered homogeneous. LST maps (figure 16) also show variability throughout the same crop due to variations in emissivity and also due to different water supplies.

5.1.3   The TES algorithm. This algorithm was developed by Gillespie *et al.* (1998), and is used to produce the Standard Products of LST and LSE from the ASTER data. The TES algorithm provides LST and LSE simultaneously and requires at least four TIR bands. It uses as input the land-leaving radiances and the downwelling atmospheric radiance, and is composed of three different modules: NEM (Normalized Emissivity Method), RATIO and MMD (Maximum–Minimum Difference). The NEM module provides an initial estimate of the surface temperature and emissivities using an iterative procedure, the RATIO module normalizes the surface emissivities providing the so-called beta spectrum, and the MMD module recovers the final surface emissivities and temperature using a semiempirical relationship between the minimum emissivity (ε_{min}) and the spectral contrast (MMD), $\varepsilon_{min} = a + b \times MMD^c$.

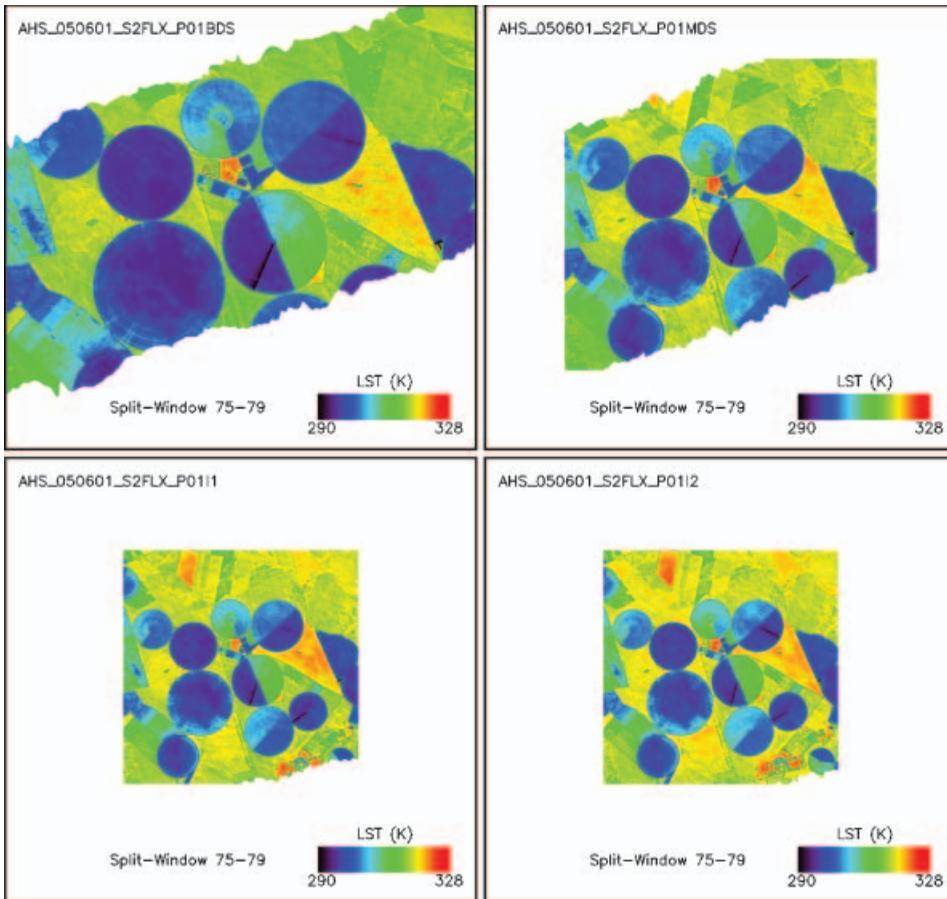The following different band configurations (Config) were considered to apply the TES method to the AHS TIR data:

Figure 16.   Land surface temperature maps obtained with the Split-Window algorithm using AHS bands 75 and 79.

$$\text{Config1}: \text{AHS bands } 75, 76, 77, 78, 79$$
$$\text{Config2}: \text{AHS bands } 72, 73, 75, 76, 77, 78, 79$$
$$\text{Config3}: \text{AHS bands } 71, 72, 73, 74, 75, 76, 77, 78, 79, 80$$

Config1 is not the optimal configuration as it uses five TIR bands, all of them located in the region 10–$12\,\mu m$. This is not the most appropriate region for calculating realistic values of the spectral contrast MMD as variations in emissivity for natural surfaces are typically low in the 10–$12\,\mu m$ region. However, this configuration was considered because it was the one used by Sobrino *et al.* (2006). Config2 is *a priori* the optimal configuration as it uses the seven optimal bands for LST retrieval, as explained in section 3.3, including bands 72 and 73 located between 8 and $9\,\mu m$. Config3 makes use of the 10 AHS TIR bands, which is *a priori* better for the calculation of the MMD, although bands 71, 74 and 80 are more affected by atmospheric absorption.

The relationship between ε_{min} and MMD must be recalculated for each band configuration. For this purpose, the 108 emissivity spectra used in the retrieval of

the TC coefficients (section 5.1.2) were used. The results of the statistical fitting are the following:

$$\text{Config1}: \ \varepsilon_{min} = 1.001 - 0.655\text{MMD}^{0.715} \rightarrow r = 0.958, \ \sigma = 0.006$$

$$\text{Config2}: \ \varepsilon_{min} = 0.999 - 0.777\text{MMD}^{0.815} \rightarrow r = 0.996, \ \sigma = 0.005$$

$$\text{Config3}: \ \varepsilon_{min} = 1.000 - 0.782\text{MMD}^{0.817} \rightarrow r = 0.997, \ \sigma = 0.004$$

where r is the correlation coefficient and σ the standard error of estimation. As expected, Config2 and Config3 provide the best results (highest r and lowest σ).

The TES algorithm was applied to the AHS imagery using the three different configurations, and the resulting LST values were tested against the 97 test points. The results are presented in figure 17. Surprisingly, the three configurations provide almost the same results, with correlations of 0.98 and bias near to 0, except for Config3, with a bias of 0.25 K. An RMSE below 1.6 K was obtained in all three cases. Differences between the three configurations were also computed for the whole images. The results (not shown here) also showed small differences between the configurations (RMSE values typically below 0.4 K), although some isolated pixels showed significant differences (between 2 and 6 K). These similarities between the results obtained with the three configurations can be explained by the low spectral contrast and high emissivity values found over the agricultural areas. In fact, all the plots considered in the test (water, corn, grass, bare soil and vineyard) had MMD values lower than 0.03, except bare soil, with an MMD of 0.04, and mean emissivity values ranging from 0.97 (bare soil) to 0.99 (corn). Therefore, the emissivity effect is in some way minimized in the Barrax area.
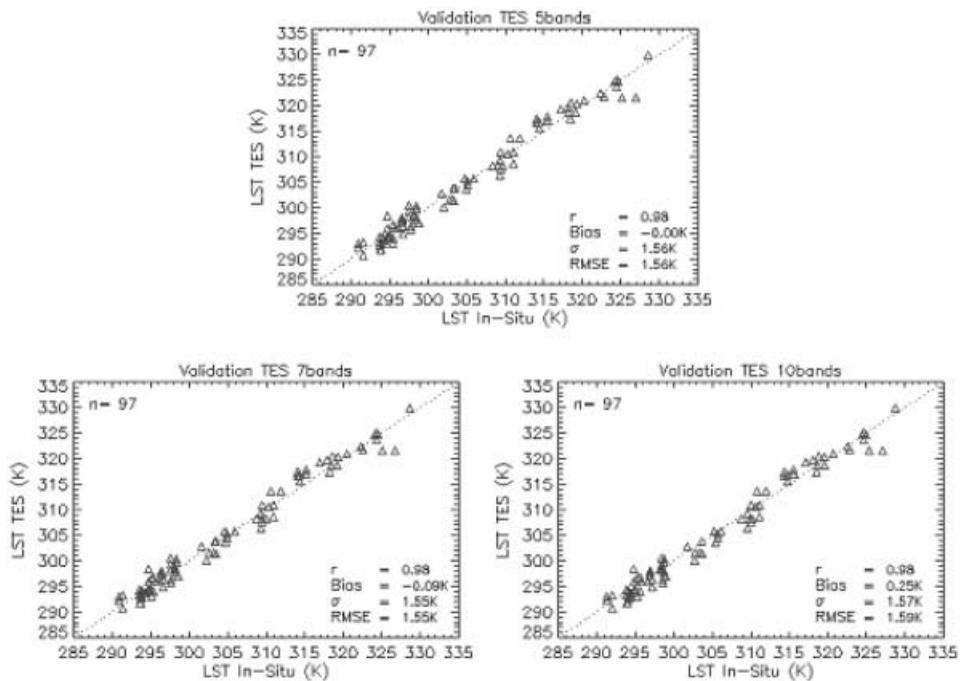

Figure 17. Validation of the TES algorithm using different AHS bands configurations against 97 *in situ* measurements (LST In-Situ) over different crops and for different dates.

   Figures 18 and 19 show the LSE (band 75) and LST maps obtained with the TES algorithm using Config2. A 'noisy' appearance of the emissivity maps in figure 18 is apparent. It should be noted that TES algorithm is very sensitive to atmospheric correction and noise of the sensor. There is also some controversy regarding the threshold applied to the MMD to distinguish between low- and high-spectral surfaces, set to 0.03 (see Gillespie *et al.* 1998). This condition seems to provoke artefacts in the images (see, for example, the discussion presented in Jiménez-Muñoz *et al.* 2006, and Sobrino *et al.* 2007). A recent recommendation proposed removing the threshold as well as the iterations in the TES algorithm (Gustafson *et al.* 2006). According to the results presented in figure 19, the noise found in emissivity maps does not appear in LST maps, at least by visual inspection. The LST maps are fairly similar to those obtained with the TC algorithm (figure 16).

5.2 *Daily evapotranspiration (ET)*

ET refers to water lost from the soil surface (evaporation) and from crops (transpiration). Knowledge of ET enables optimization of water use for irrigation, and estimation of ET by solving the energy balance equation requires the availability of TIR data.

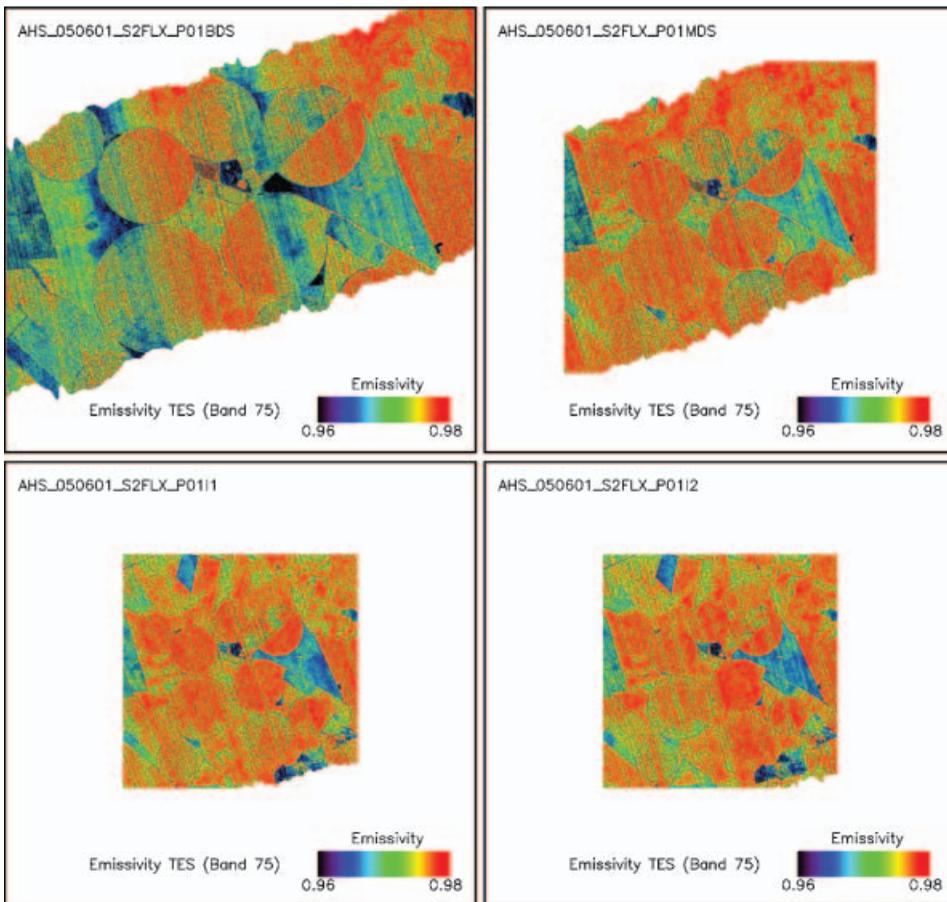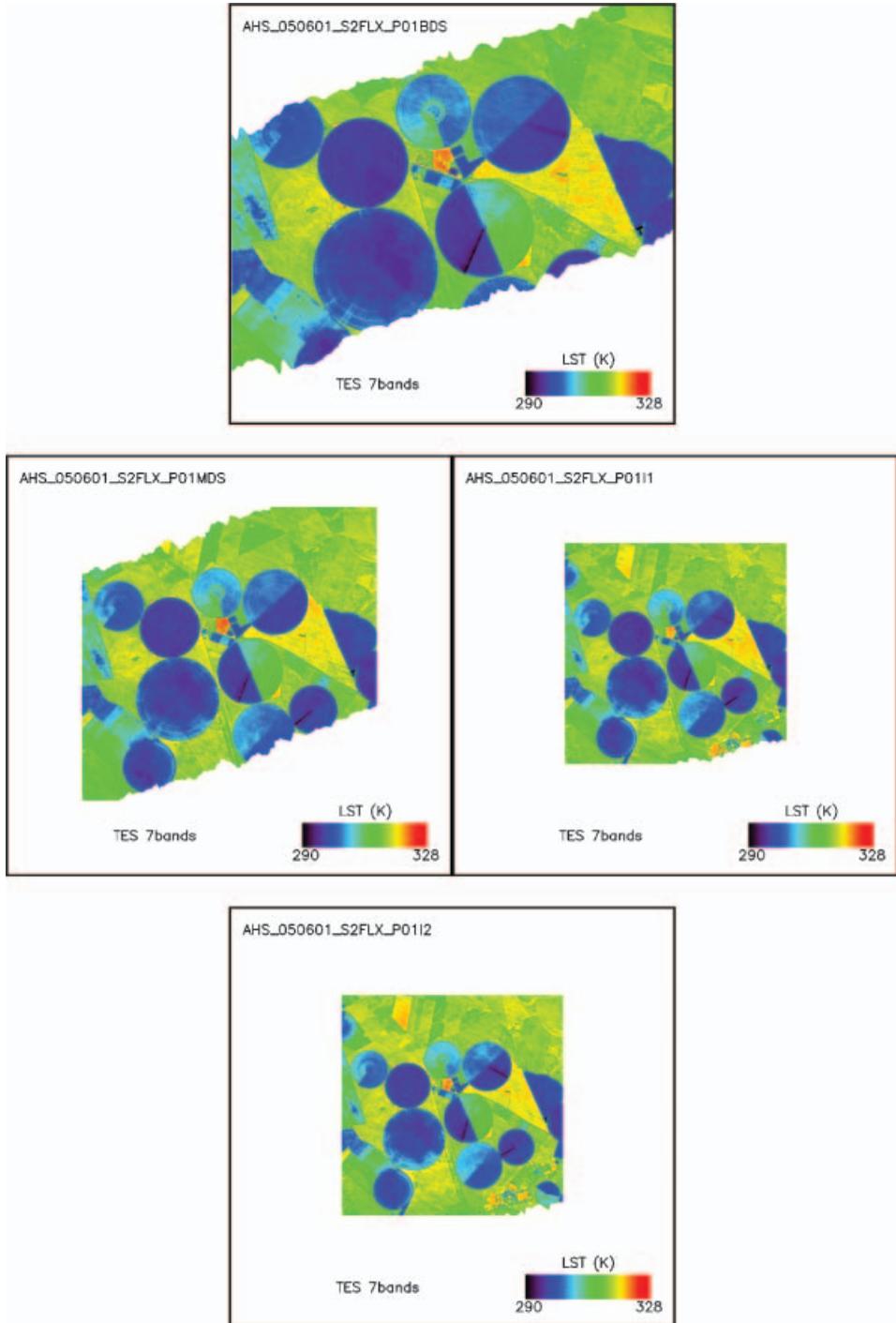Figure 18. Land surface emissivity maps for AHS band 75 obtained with the TES algorithm.

Figure 19. Land surface temperature maps obtained with the TES algorithm.

In this study, daily ET was retrieved according to the methodology presented in Gómez *et al.* (2005) and Sobrino *et al.* (2005), which is based on the Simplified Surface Energy Balance Index (S-SEBI) model (Roerink *et al.* 2000). The

instantaneous evapotranspiration (ET_i) is given by:

$$LET_i = \Lambda_i (R_{ni} - G_i) \tag{9}$$

where L is the latent heat of vaporization ($2.45\,\mathrm{MJ\,kg^{-1}}$), Λ is the evaporative fraction, R_n is the net radiation and G is the soil heat flux. The subscript 'i' refers to 'instantaneous' values and the subscript 'd' is used for 'daily' values. Then, daily ET (ET_d) can be obtained as:

$$ET_d = \frac{\Lambda_i C_{di} R_{ni}}{L} \tag{10}$$

where C_{di} is the ratio between daily and instantaneous R_n, $C_{di} = R_{nd}/R_{ni}$ (Seguin and Itier 1983; Wassenaar *et al.* 2002), which is day and year dependent (Bastiaanssen *et al.* 2000). This was estimated from measurements of net radiation registered in a meteorological station located in the Barrax area. In the step from equation (9) to equation (10), the assumption $\Lambda_i \approx \Lambda_d$ and $G_d \approx 0$ was considered.

Instantaneous net radiation (R_{ni}) is obtained from the balance between the incoming and outgoing shortwave and longwave radiation:

$$R_{ni} = (1 - \alpha_s) R^{\downarrow}_{sw} + \varepsilon R^{\downarrow}_{lw} - \varepsilon \sigma T_S^4 \tag{11}$$

where α_s is the surface albedo, $R^{\downarrow}_{sw}$ and $R^{\downarrow}_{lw}$ are, respectively, shortwave and longwave incoming radiation (measured at meteorological stations), ε and T_s are, respectively, surface emissivity and temperature (estimated with any of the methods presented in the previous section) and σ is the Stefan–Boltzmann constant ($5.670 \times 10^{-8}\,\mathrm{W\,m^{-2}\,K^{-4}}$). The surface albedo was estimated from a weighted mean of at-surface reflectivities ($\rho^{surface}$) estimated with AHS VNIR atmospherically corrected bands:

$$\alpha_s = \sum_{i=1}^{20} \omega_i \rho_i^{surface} \tag{12}$$

where ω_i ($i = 1$–20) are the weight factors obtained from the solar irradiance spectrum at the top of the atmosphere (see table 6). Finally, the evaporative fraction is estimated as:

$$\Lambda_i = \frac{T_H - T_s}{T_H - T_{LET}} \tag{13}$$

where T_H and T_{LET} are two characteristic temperatures obtained from the plot of surface temperature versus surface albedo (Roerink *et al.* 2000).

The methodology was applied to the AHS imagery, and the daily ET values extracted from the images were compared to those measured *in situ* in the lysimeter station located in the green grass plot (festuca, L13). The results of the test are shown in table 7, in which an RMSE of ~1 mm/day is obtained. The values measured at the lysimeter station on 13 and 14 July were not available because of a technical problem. Table 7 shows that ET_d values for near consecutive flights are almost the same, but ET_d values along the same day are not constant, with differences ranging between 1.3 and 1.9 mm/day. This indicates that some errors are expected when a temporal integrated value of ET is obtained from instantaneous values by means of the radio C_{di} because daily ET refers to a unique value for a certain day.

Table 6. Weight factors (ω_i) used in the estimation of surface albedo according to equation (12).

AHS band	λcentre (μm)	$S^{\downarrow}$ (W m^{-2} μm^{-1})	ω_i
1	0.455	1923.1	0.073
2	0.484	1886.8	0.072
3	0.513	1829.1	0.070
4	0.542	1774.3	0.068
5	0.571	1740.5	0.067
6	0.601	1689.2	0.065
7	0.630	1602.5	0.061
8	0.659	1510.0	0.058
9	0.689	1403.9	0.054
10	0.718	1324.1	0.051
11	0.746	1240.6	0.047
12	0.774	1152.4	0.044
13	0.804	1089.5	0.042
14	0.833	1014.9	0.039
15	0.862	952.5	0.036
16	0.891	894.5	0.034
17	0.918	842.9	0.032
18	0.948	806.4	0.031
19	0.975	767.2	0.029
20	1.004	726.0	0.028

$S^{\downarrow}$, solar irradiance at the top of the atmosphere.

Figure 20 includes some illustrative daily ET maps for the images acquired on 1 June 2005. The ET values range between approximately 0 and 10 mm/day, with bare soil and senescent vegetation providing the lowest values, and green vegetation providing the highest ones, as expected. ET values for flights BDS and MDS (1123 and 1148 GMT, respectively) are higher than those for flights I1 and I2 (1211 and 1233 GMT, respectively), which also shows the unexpected variations in ET$_d$ along the day, as noted earlier. The ET maps also show the irrigation patterns.

6. Summary and conclusions

Field campaigns, like the SEN2FLEX campaign, provide an excellent opportunity for collecting different ground-based measurements and also for validating different algorithms for the retrieval of biogeophysical parameters from remote sensing data of interest in environmental studies.

In this paper we have focused on the analysis of thermal remote sensing data acquired by the AHS sensor, with 10 thermal bands in the range 8–13 μm, which allows the retrieval of LST, LSE and ET in combination with VNIR bands. A vicarious calibration of the AHS TIR bands was previously considered, showing errors below 1.5 K. Three methods for LST retrieval using different TIR bands configurations were tested: SC (one band), TC (two bands) and TES (five, seven and 10 bands). In the SC method a constant emissivity was assumed (0.98), whereas in the TC method surface emissivities were estimated from the NDVI approach. The methods were validated against 97 test points, with RMSE values of 1.7, 1.8 and 1.6 K for the SC, TC and TES methods, respectively. Note that the accuracy on the LST retrieval is limited by the error obtained in the vicarious calibration. The small differences in the RMSE values do not allow us to conclude that one method is

Table 7. Comparison between daily evapotranspiration (ET$_d$) obtained from AHS imagery and that measured *in situ* over the lysimeter station located in the green grass (L13) plot. Values of the ratio between daily and instantaneous net radiation (C_{di}) obtained from measurements in the meteorological station and relationships between temperatures T_H and T_{LET} and surface albedo (α_s) are also given.

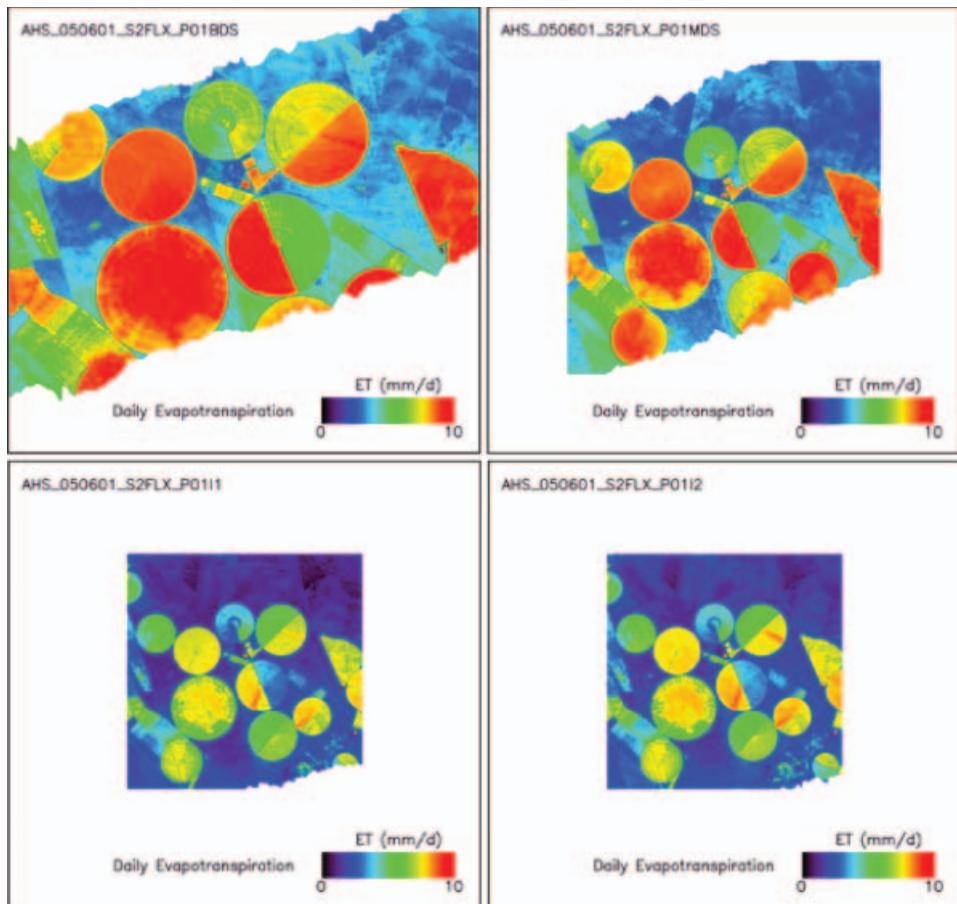| Date	Flight	Time (GMT)	C_{di}	T_H and T_{LET} (K)	ET$_d$ AHS (mm/day)	ET$_d$ situ (mm/day)	AHS situ (mm/day)
050601	BDS	11:23	0.52	$T_H=-50\alpha_s+345$ $T_{LET}=10\alpha_s+286$	6.9	6.1	0.8
050601	MDS	11:48	0.49	$T_H=-50\alpha_s+342$ $T_{LET}=12.5\alpha_s+287$	6.6	6.1	0.5
050601	I1	12:11	0.45	$T_H=-45\alpha_s+342$ $T_{LET}=12.5\alpha_s+287$	5.3	6.1	−0.8
050601	I2	12:33	0.44	$T_H=-50\alpha_s+344$ $T_{LET}=12.5\alpha_s+286$	5.3	6.1	−0.8
050602	BDS	11:19	0.49	$T_H=-50\alpha_s+345$ $T_{LET}=17.5\alpha_s+287$	6.5	4.7	1.8
050602	MDS	11:41	0.45	$T_H=-52.5\alpha_s+345$ $T_{LET}=10\alpha_s+290$	6.5	4.7	1.8
050602	I1	12:03	0.43	$T_H=-50\alpha_s+345$ $T_{LET}=12.5\alpha_s+290$	5.1	4.7	0.4
050602	I2	12:25	0.40	$T_H=-47.5\alpha_s+347$ $T_{LET}=15\alpha_s+289$	5.1	4.7	0.4
050603	BDS	11:11	0.53	$T_H=-55\alpha_s+350$ $T_{LET}=12.5\alpha_s+290$	6.3	6.0	0.3
050603	MDS	11:34	0.50	$T_H=-50\alpha_s+350$ $T_{LET}=12.5\alpha_s+291$	6.0	6.0	0.0
050603	I1	11:57	0.45	$T_H=-50\alpha_s+350$ $T_{LET}=12.5\alpha_s+291$	4.4	6.0	−1.6
050603	I2	12:19	0.44	$T_H=-52.5\alpha_s+351$ $T_{LET}=12.5\alpha_s+291$	4.4	6.0	−1.6
050712	BDS	11:56	0.46	$T_H=-67.5\alpha_s+364$ $T_{LET}=10\alpha_s+294$	6.2	5.3	0.9
050712	MDS	12:21	0.45	$T_H=-57.5\alpha_s+360$ $T_{LET}=12.5\alpha_s+294$	6.3	5.3	1.0
					Bias		0.2
					St. Dev.		1.1
					RMSE		1.1

Figure 20.   Daily evapotranspiration maps.

better than the other, which could lead to the conclusion that an improvement in LST retrieval is not achieved when multispectral TIR data are used. However, some observations should be emphasized to avoid inaccurate conclusions:

(1) SC methods provide good results only with a low atmospheric water vapour content, as described by Sobrino and Jiménez-Muñoz (2005). In this study, and for the flight altitudes, water vapour values were less than 1 g/cm^2, which explains the good performance of the SC method. Furthermore, the assumption of a constant value for emissivity is only acceptable over areas with high emissivities and low value variations, as is the case in agricultural areas such as the Barrax site (with emissivity values ranging between about 0.97 and 0.99).

(2) TC methods provide good results in global atmospheric conditions (except for a very low atmospheric water vapour content, for which the SC method can provide more accurate results, as indicated also by Sobrino and Jiménez-Muñoz, 2005). However, the main constraint is that prior knowledge of the emissivity is required. If multispectral TIR data are not available, surface emissivities can be only estimated from VNIR bands, for example using a simple approach with the NDVI. However, this method requires prior

knowledge of soil emissivity, and shows some problems over certain surfaces such as water or senescent vegetation (which could be solved using ancillary information).

(3) Although the TES algorithm is designed to work over all kinds of natural surfaces, it is especially useful over areas with high spectral contrast. The Barrax area has high emissivity values with low spectral contrast, so it is more or less logical to expect similar results regardless of the number of TIR bands used because the emissivity effect is not important over these kinds of areas. The main constraint with the TES algorithm is that a precise atmospheric correction is needed. However, if multispectral TIR data are available, different atmospheric correction methods based on the image itself could be applied, such as the Autonomous Atmospheric Compensation (AAC; Gu *et al.* 2000) or In-Scene Atmospheric Compensation (ISAC) (Young *et al.* 2002) algorithms.

The availability of TIR data also allows the estimation of heat fluxes and ET by solving the energy balance equation. In this paper we have presented a simple methodology for daily ET retrieval, in which instantaneous values are converted to daily values using a time-dependent coefficient. The method was tested against values measured in a lysimeter station located in the grass (festuca) plot. The results are acceptable, with an RMSE of around 1 mm/day, but some variations in the daily ET obtained with different images acquired during the same day were found.

With the results presented in this paper we hope to modestly contribute to the scientific discussion regarding the usefulness of TIR data and their availability in future sensors.

Acknowledgements

References

BALICK, L.K., JEFFERY, C.A. and HENDERSON, B.G., 2003, Turbulence-induced spatial variation of surface temperature in high-resolution thermal IR satellite imagery. *Proceedings of SPIE*, **4879**, pp. 221–230.

BASTIAANSSEN, W.G.M., MOLDEN, D.J. and MAKIN, I.W., 2000, Remote sensing for irrigated agriculture: examples from research and possible applications. *Agricultural Water Management*, **46**, pp. 137–155.

BERK, A., ANDERSON, G.P., ACHARYA, P.K., CHETWYND, J.H., BERNSTEIN, L.S., SHETTLE, E.P., MATTHEW, M.W. and ADLER-GOLDEN, S.M., 1999, *MODTRAN4 User's Manual* (Hanscom AFB, MA: Air Force Research Laboratory).

CARLSON, T.N. and RIPLEY, D.A., 1997, On the relation between NDVI, fractional vegetation cover, and leaf area index. *Remote Sensing of Environment*, **62**, pp. 241–252.

GILLESPIE, A., ROKUGAWA, S., MATSUNAGA, T., COTHERN, J.S., HOOK, S. and KAHLE, A.B., 1998, A temperature and emissivity separation algorithm for advanced spaceborne thermal emission and reflection radiometer (ASTER) images. *IEEE Transactions on Geoscience and Remote Sensing*, **36**, pp. 1113–1126.

GÓMEZ, M., SOBRINO, J.A., OLIOSO, A. and JACOB, F., 2005, Retrieval of evapotranspiration over the Alpilles/ReSeDA experimental site using airborne POLDER sensor and thermal camera. *Remote Sensing of Environment*, **96**, pp. 399–408.

GU, D., GILLESPIE, A.R., KAHLE, A.B. and PALLUCONI, F.D., 2000, Autonomous Atmospheric Compensation (AAC) of high resolution hyperspectral thermal infrared remote-sensing imagery. *IEEE Transactions on Geoscience and Remote Sensing*, **38**, pp. 2557–2570.

GUANTER, L., RICHTER, R., ALONSO, L. and MORENO, J., 2005, Atmospheric correction algorithm for remote sensing data over land. II. Application to ESA SPARC campaigns: airborne sensors. In *Proceedings of the SPARC*, 4–5 July, Enschede, the Netherlands (Noordwijk, The Netherlands: ESA Publications Division), WPP-250, pp. 770–775.

GUSTAFSON, W.T., GILLESPIE, A.R. and YAMADA, G., 2006, Revisions to the ASTER temperature/emissivity separation algorithm. In *Recent Advances in Quantitative Remote Sensing*, J.A. Sobrino (Ed.), 25–29 September, Torrent (Valencia), Spain (Spain: Publicacions de la Universitat de València).

JIMÉNEZ-MUÑOZ, J.C. and SOBRINO, J.A., 2006, Emissivity spectra obtained from field and laboratory measurements using the temperature and emissivity separation algorithm. *Applied Optics*, **45**, pp. 7104–7109.

JIMÉNEZ-MUÑOZ, J.C., SOBRINO, J.A., GILLESPIE, A., SABOL, D. and GUSTAFSON, W.T., 2006, Improved land surface emissivities over agricultural areas using ASTER NDVI. *Remote Sensing of Environment*, **103**, pp. 474–487.

KERR, Y.H., LAGOUARDE, J.P., NERRY, F. and OTTLÉ, C., 2004, Land surface temperature retrieval techniques and applications: case of the AVHRR. In *Thermal Remote Sensing in Land Surface Processes*, D.A. Quattrochi and J.C. Luvall (Eds), pp. 33–109 (Boca Raton, FL: CRC Press).

MORENO, J., CASELLES, V., MARTÍNEZ-LOZANO, J.A., MELIÁ, J., SOBRINO, J.A., CALERA, A., MONTERO, F. and CISNEROS, J.M., 2001, The measurements programme at Barrax. In *DAISEX Final Results Workshop*, 15–16 March (The Netherlands: ESTEC, ESA Publications Division), SP-499, pp. 43–51.

QUATTROCHI, D.A. and LUVALL, J.C., 1999, Thermal infrared remote sensing data for analysis of landscape ecological processes: methods and applications. *Landscape Ecology*, **14**, pp. 577–598.

ROERINK, G., SU, Z. and MENENTI, M., 2000, S-SEBI: a simple remote sensing algorithm to estimate the surface energy balance. *Physics and Chemistry of the Earth (B)*, **25**, pp. 147–157.

SEGUIN, B. and ITIER, B., 1983, Using midday surface temperature to estimate daily evaporation from satellite thermal IR data. *International Journal of Remote Sensing*, **4**, pp. 371–383.

SOBRINO, J.A., GÓMEZ, M., JIMÉNEZ-MUÑOZ, J.C., OLIOSO, A. and CHEHBOUNI, G., 2005, A simple algorithm to estimate evapotranspiration from DAIS data: application to the DAISEX campaigns. *Journal of Hydrology*, **315**, pp. 117–125.

SOBRINO, J.A. and JIMÉNEZ-MUÑOZ, J.C., 2005, Land surface temperature retrieval from thermal infrared data: an assessment in the context of the Surface Processes and Ecosystem Changes Through Response Analysis (SPECTRA) mission. *Journal of Geophysical Research*, **110**, pp. D16103, doi: 10.1029/2004JD005588.

SOBRINO, J.A., JIMÉNEZ-MUÑOZ, J.C., BALICK, L., GILLESPIE, A., SABOL, D. and GUSTAFSON, W.T., 2007, Accuracy of ASTER level-2 thermal-infrared standard products of an agricultural area in Spain. *Remote Sensing of Environment*, **106**, pp. 146–153.

SOBRINO, J.A., JIMÉNEZ-MUÑOZ, J.C., ZARCO-TEJADA, P.J., SEPULCRE-CANTÓ, G. and DE MIGUEL, E., 2006, Land surface temperature derived from airborne hyperspectral scanner thermal infrared data. *Remote Sensing of Environment*, **102**, pp. 99–115.

SOBRINO, J.A. and RAISSOUNI, N., 2000, Toward remote sensing methods for land cover dynamic monitoring: application to Morocco. *International Journal of Remote Sensing*, **21**, pp. 353–366.

TOONOKA, H., PALLUCONI, F.D., HOOK, S.J. and MATSUNAGA, T., 2005, Vicarious calibration of ASTER thermal infrared bands. *IEEE Transactions on Geoscience and Remote Sensing*, **432**, pp. 1113–1126.

WASSENAAR, T., OLIOSO, A., HASAGER, C., JACOB, F. and CHEHBOUNI, A., 2002, Estimation of evapotranspiration on heterogeneous pixels. In *Recent Advances in Quantitative Remote Sensing*, J.A. Sobrino (Ed.), Torrent (Valencia), Spain, 16–20 September (Spain: Publicacions de la Universitat de València), pp. 458–465.

YOUNG, S.J., JOHNSON, B.R. and HACKWELL, J.A., 2002, An in-scene method for atmospheric compensation of thermal hyperspectral data. *Journal of Geophysical Research*, **107**, doi: 10.1029/2001JD001266.